Solid State Communications 350 (2022) 114740

Contents lists available at ScienceDirect

Solid State Communications

journal homepage: www.elsevier.com/locate/ssc

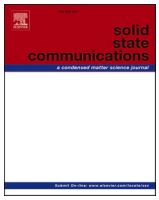

Sn doping effects on the structural, microstructural, Seebeck coefficient, and photocatalytic properties of ZnO thin films

Sabrina Roguai [a,b,*], Abdelkader Djelloul [a,b]

[a] LASPI²A Laboratoire des Structures, Propriétés et Interactions Inter Atomiques, Université Abbes Laghrour, Khenchela 40000, Algeria
[b] Science of Matter, Abbes Laghrour University, Khenchela, Algeria

ARTICLE INFO

Communicated by Prof. F. Peeters

Keywords:
Sn-doped ZnO films
Pneumatic spray
Photocatalyst
Methylene blue

ABSTRACT

Successful ZnO, $Sn_xZn_{1-x}O$ [x = 0.01 and 0.03] films were synthesized by pyrolysis on glass substrates at *Ts* = 450 °C for 1 h. Sn doping effect on structural, microstructural, Seebeck coefficient and optical characterizations were performed. It found that all films crystallize in the hexagonal würtzite structure. The success of the 1 at.% Sn doping is confirmed by the SEM images which show that the microstructure of the 1 at.% Sn doped ZnO is rather similar to that of the undoped ZnO film and shows spherical grains, by further increasing the Sn content (3 at.%), the films show a small spherical grains. Through FTIR analysis, distinct characteristic absorption peak at 449 cm^{-1} for the Zn–O stretching mode with some changes in intensities. ZnO, ZnO:Sn films transmit decrease from 87 to 66% with doping content, while the bandgap energy not affected with doping. The Seebeck coefficient decreases from |188| to |110|μV/K, while the carrier concentration increases from 3.37 × 10^{18} and 1.00 × $10^{19}cm^{-3}$ with doping content. The photocatalytic activity of $Zn_{1-x}Sn_xO$ investigated by testing the degradation of methylene blue (MB).

1. Introduction

ZnO thin films are of great interest due to its special characteristics, such as non-toxicity, abundance in nature, high chemical and thermal stability and direct band gap (3.3 eV) [1]. These benefits are of immense importance in different domains such as gas sensors [2], piezoelectrical devices [3], surface acoustic wave devices [4] and solar cells [5,6].

Nevertheless, the surface conductance of this material is affected by chemisorptions and oxygen adsorptions. The electronic and optical characteristics of this material have been investigated by several scientists for specific uses [7]. The electrical and optical characteristics of various ZnO-doped metal ions have been analyzed [7,8].

Many types of dopants have been used (Al, In, As, S, Sn, Mn, etc. [9,10]) for many important applications in ZnO thin films, these dopant elements offer a manner to regulate the electrical, optical, and magnetic properties, which make doped ZnO films promising candidates as high conductivity and transparency conductors in visible light range.

The Zinc oxide doped with Sn can increase the optical, electrical and structural properties of ZnO thin films [11,12]. As Sn^{4+} replaces Zn^{2+} in the ZnO crystal structure, two more free electrons are capable of participating in electrical conduction. Due to their nearly identical radius, Zn can be easily substituted by Sn without causing significant lattice distortion.

TZO Thin films elaborated by the spray pyrolysis technique indicate that the optical properties of this system are not affected by the doping. While for the structural properties, the crystallite size increased with doping and reached a maximum value (42 nm) at 3 at.% doping [8]. Another study utilizing the same doping technique reported that the crystallite size attained a value of 95 nm at 2 at.% and 3 at.% doping, resulting in greater porosity values [13]. Recent works, thin films of Zn1-xSnxO (x ≤ 10 at.%) indicates that the doping influence on the optical properties that it observing a decrease in the values of the bandgap energy from 3.26eV to 2.96eV. To the structural and microstructural, it shows a decrease in crystallite size values (50-26 nm, XRD) and the grain size (280-60 nm, SEM and AFM) [14].

Thanks to these properties, TZO thin films have several applications such as sensing applications [15], optoelectronic applications [16], dyesensi-tizedsolarcells (DSSC) [17,18]. Transparent electrode materials [19] or anti-reflecting coatings (ARC) in semiconductor solar cells [20], photocatalytic activity [21].

Various deposition methods can be used to synthesize ZnO:Sn thin films, such as sol-gel [22], electron deposition [23], spray pyrolysis

* Corresponding author. LASPI²A Laboratoire des Structures, Propriétés et Interactions Inter Atomiques, Université Abbes Laghrour, Khenchela 40000, Algeria.
E-mail address: rog.sabrina@yahoo.fr (S. Roguai).

https://doi.org/10.1016/j.ssc.2022.114740
Received 27 May 2021; Received in revised form 14 March 2022; Accepted 16 March 2022
Available online 7 April 2022

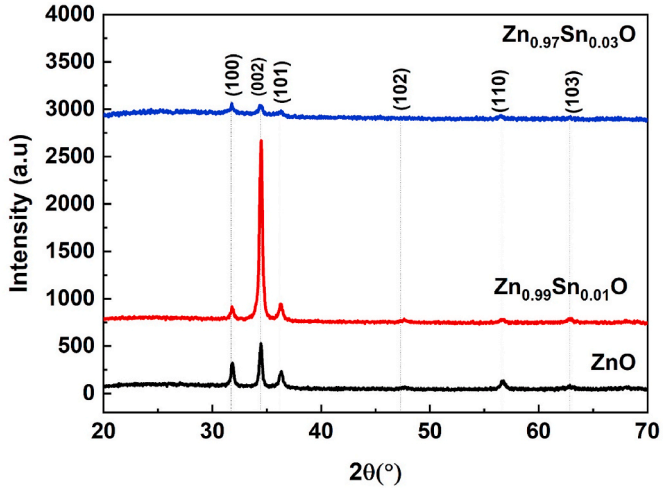

Fig. 1. X-ray diffraction patterns of Sn-doped ZnO thin films with different Sn concentrations.

[24], chemical vapor [25], pulsed layer [26] and thermionic vacuum arc [27]. Among these methods, the pneumatic spray pyrolysis has the advantage of low cost and easy preparation of metal oxide semiconductors. The goal of this study is to obtain high photocatalyst ZnO:Sn thin layers for methylene blue degradation (MB), deposited on glass substrates by pneumatic spray pyrolysis technique, and to find out the effect of Sn content on their Seebeck coefficient, optical, structural, and microstructural properties.

2. Experimental part

2.1. Pneumatic spray pyrolysis

$Zn_{1-x}Sn_xO$ [x = 0.00, 0.01 and 0.03] thin films deposited by pneumatic spray pyrolysis technique, using an air compressor [28], were grown on 30 × 10 Cm^2 glass substrates ultrasonically cleaned. These latter were rinsed with acetone followed by deionized water and finally dried at room temperature. The precursor solutions were prepared using zinc acetate ($C_4H_6O_4Zn \cdot 2H_2O$) (Fulka99.9%); and tin chloride ($SnCl_2$) (Fulka 99.9%); as the source material for Zn and Sn. Firstly, 1.2g of dehydrate zinc acetate was dissolved in 30 ml of methanol (Merck 99.5%) and stirred for 30 min using a magnetic stirrer at ambient temperature to obtain a clear and homogeneous solution. Then, $SnCl_2$ was added as Sn^{4+} metal ions source in molar (Sn/Zn) ratio of 1 at.%, and 3 at.%. The solution was finally mixed for 30min using a magnetic stirrer. For film deposition, the main deposition settings were 450 °C, 20 ml/h, 20 cm, 1.5atm and 1 h for temperature, sputtering rate, nozzle-to-substrate distance, air pressure and the deposit time, respectively.

2.2. Characterization techniques

Various parameters of the so-obtained Sn-doped ZnO thin films were examined. The crystallinity was investigated via X-ray diffraction (XRD) in 25–70° range using Cu Kα radiation (1.5418 Å), by means of PANalytical Empyrean diffractometer. Surface morphology of films was characterized by scanning electron microscopy (SEM), carried out with a JEOL JSM 7500F microscope. The infrared absorption (FTIR) spectra were recorded to examine the structure using Thermo-Nicolet equipment in 4000–400 cm^{-1} region. The transmittance was recorded in wavelength range of 190–1100 nm with Parkin Elmer UV-VIS-NIR Lambda 19 spectrophotometer. The Seebeck coefficient was calculated on the basis of detected Seebeck voltage and temperature gradient range difference from zero to 160 K with 20 K steps.

2.3. Photocatalytic experiments

Photocatalytic activity of $Zn_{1-x}Sn_xO$ thin films [X = 0.00, 0.01 and 0.03] was evaluated by measuring MB decolorization under UV-light irradiation at room temperature, using a 100 W incandescent lamp. The photocatalyst and MB solution were placed in 250 ml beaker for 30 min with stirring in the dark to reach the adsorption-desorption equilibrium of MB on the catalyst surface pretreated the solutions. Afterwards, the solutions were irradiated each 30 min, and the concentration of MB was determined by recording the changes in the maximum absorption band of MB (664 nm), using Parkin Elmer UV-VIS-NIR Lambda spectrophotometer 19.

3. Results and discussion

3.1. Structural properties

The X-ray diffraction patterns of $Zn_{1-x}Sn_xO$ [x = 0.0, 0.01, and 0.03] thin films (Fig. 1.), correspond to three main diffraction peaks of ZnO, (100), (002), (101), (102), (110) and (103). All observed peaks were attributed to hexagonal wurtzite polycrystalline structure according to (JCPDS 36–1451), with lattice parameters: a = b = 3.251 Å, c = 5.320 Å and the space group $P6_3mc$ [29–32]. No additional phases corresponding to SnO and SnO_2were formed.

Moreover, it noticed that the obtained TZO layers were preferentially oriented along the (002) direction [33]. This revealed a complete dissolution of Sn in the ZnO crystal lattice by occupying the ionic sites of Zn. The relative intensity of diffraction peaks decreased with increasing Sn content.

From the condition of substitutional solid solution (S.S) by W. Hume-Rothery, the difference between the ionic radii and the dopant lattice must be less than 15% for the dopant to be incorporated. In our study, the ionic radii values of Zn^{2+} and Sn^{4+} were 0.74 Å and 0.69 Å respectively, so the substitution of these dopants with Zn^{2+} was feasible in the film lattice [34].

Also, the intensity of this preferential peak (002) increased to a maximum value that indicated an improvement in the c-axis orientation of ZnO thin films for a doping content of x = 0.01 [35], this could be attributed to the lowest surface energy, since the hexagonal structure, which is the c-plane of ZnO crystallites, is the one that matches to the most densely packed plane [36]. In the contrary, intensity decreased directly when tin doping content exceeded 1 at.%, which showed that the crystallinity of the films was affected. This result might be explained by the formation of stresses due to the difference in ion radius between zinc and tin [37].

In addition, the peak position of (002) plane was shifted heterogeneously according to the doping rate 2θ = 34.46, 34.49, and 34.41°, for the concentrations of x = 0.00, 0.01, and 0.03 respectively. For 1 at.% doping content, the peak position of the (002) plane was shifted to the high 2θ value. This could be attributed to the fact that the ionic radius of Sn^{4+} is smaller than that of Zn^{2+}leads to an increase in the diffraction angle (002) and a slight reduction in the interplanar spacing (d (002)) [38]. However, for a doping content of 3 at.%, the peak (002) shifted to an angle (2θ) lower than that of pure ZnO thin films this may possibly interpreted by the influence of the experimental conditions and the deposition method (pneumatic spray) In other hand due to the difference in ionic radius.

The crystallite size of $Zn_{1-x}Sn_xO$ thin films were calculated using Debye– Scherrer formula [39,40]:

$$D = \frac{0.9\lambda}{\beta cos\theta} \quad (1)$$

where D is the grain size of the crystallites, λ is the X-ray wavelength, β is the full width half maxima and θ is the Bragg diffraction angle. The determined crystallite sizes were changed by varing Sn doping from 0 at.

Table 1
X-ray difraction data (d-spacing, FWHM, cell parameters 'a' and 'c', c/a ratio, average crystallite size (D) and micro-strain (ε) of diferent $Zn_{1-x}Sn_xO$ thin films).

Sample	d (Å)	FWHM	a (Å)	c (Å)	c/a	D (nm)	$\varepsilon \times 10^{-3}$	$\delta \times 10^{-4}$
ZnO	2.6024	0.2657	3.249	5.204	1.601	36	5.57	7.52
$Zn_{0.99}Sn_{0.01}O$	2.6004	0.2657	3.243	5.200	1.603	36	5.47	7.55
$Zn_{0.97}Sn_{0.03}O$	2.6061	0.2362	3.249	5.212	1.604	41	4.86	5.98

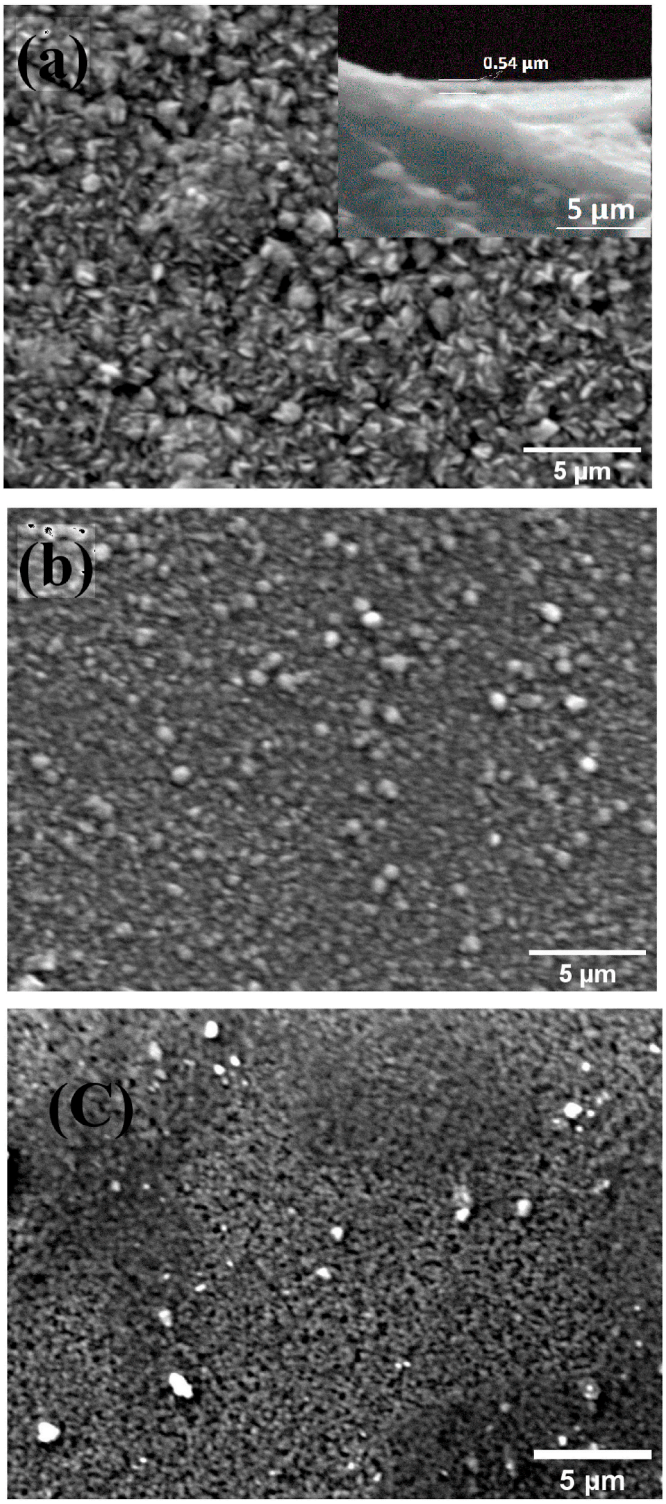

Fig. 2. SEM images of undoped film (a), 1 at.% Sn-doped ZnO films (b), and 3 at.% Sn-doped sample (c).

% to 3 at.%. Table 1 illustrates that the crystallite size is reduced with increasing Sn content, except for that of 3 at.%.

The film lattice parameters were defined by formula (2) [41]:

$$\frac{1}{d^2}=\frac{4}{3}\left(\frac{h^2+hk+k^2}{a^2}\right)+\left(\frac{l^2}{c^2}\right) \quad (2)$$

where a and c are the lattice parameters, h k l, are the miller indices and d is the interplanar distance for the atoms. It may be noted that no changes in the lattice parameters were observed in the doped thin films (Table 1). The X-ray patterns indicated clearly that the pure and Sn-doped ZnO films presented a good crystalline nature.

Also, for the wurtzite structure, the significance of the c/a ratio is judged to be 1.633 [42], in our paper, the c/a ratio revealed values results in the range of 1.601 and 1.604, which could mean the creation of oxygen on the interstitial sites and zinc vacancies (V_{Zn}) [43].

From the present structural studies, we have also estimated the lattice strain of the samples by using the following relation [44]:

$$\varepsilon=\frac{\beta cos\theta}{4} \quad (3)$$

Table 1, shows the values of lattice strain of pure and Sn-doped samples which decreases from 6.34 $\times$ 10^{-3} to 5.56 $\times$ 10^{-3} for pure ZnO and 3% Sn-doped ZnO successively, this confirms the incorporation of Sn into ZnO films.

The dislocation density (δ) of the obtained films has been calculated using the following equation [45]:

$$\delta=\frac{1}{D^2} \quad (4)$$

The dislocation density of the samples was slightly higher (7.55 $\times$ 10^{-4}) for 1% Sn–ZnO compared to pure ZnO (7.52 $\times$ 10^{-4}) confirming the incorporation of Sn ions in ZnO, then reduced to 5.98 $\times$ 10^{-4} for 3 at.%Sn–ZnO indicating an impact structure due to the substitution of Sn^{4+} in the ZnO lattice.

3.2. Surface morphological properties

The surface morphologies of prepared thin films are shown in Fig. 2. As can be seen in the images, ZnO and TZO films were polycrystalline, continuous (no pores were observed), and consisted of nanosized grains. The microstructure of the 1% Sn-doped ZnO was rather similar to that of the undoped ZnO films and had spherical grains. Both films have smaller spherical grains by increasing the Sn content to 3 at.%.

At 3% doping level, the grain size seemed to be decreased compared to 1 at.% doping level, which suggests a decline in crystalline properties. This might be assigned to the concentration limit of Sn doping in the ZnO lattice.

3.3. The chemical composition properties

The chemical composition of the thin films deposited on a glass substrate was determined by energy dispersive X-ray spectroscopy analysis. The EDAX spectrum (Fig. 3) collected below 20 keV indicated the existence of Zn, Sn and O in the thin film. The Si peak originates in the glass substrate [31]. The EDAX analysis, as reported in Table 2, showed a perfect correlation between expected doping level and Sn/Zn content extracted from the EDAX spectra. This indicated a full doping process and a high purity films with uniform doping concentration in

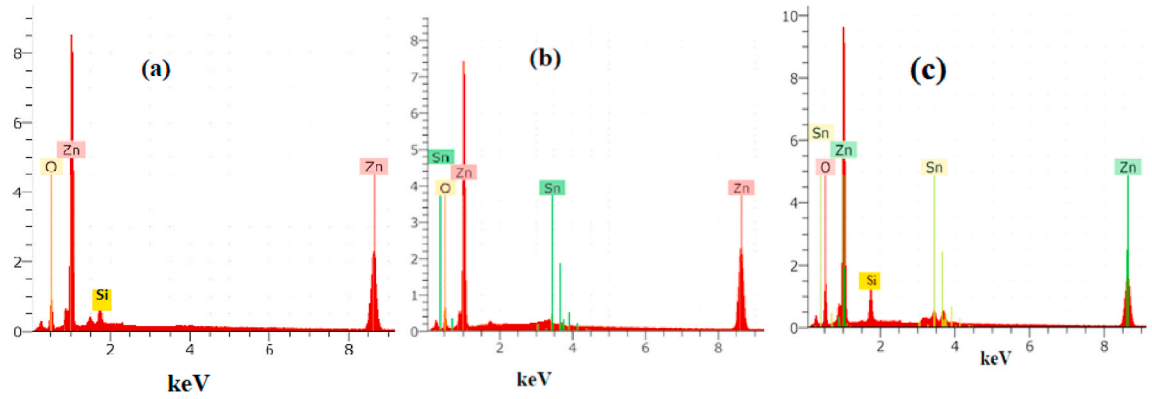

Fig. 3. EDAX elemental composition analysis of a pure ZnO flm and b–d Sn–doped Zn1−xSnxO thin flms. The images b–d correspond to the Sn atomic content of 1 at. %, and 3 at.%, respectively.

Table 2
Thin film composition and stoichiometry obtained by statistical analysis of EDAX spectra.

$Zn_{1-x}Sn_xO$ "Nominal" Sn content (at)	Zn (at. %)	Sn (at. %)	O (at. %)	x (Sn) "EDS" Sn content (at)
ZnO	72.42	/	27.58	0
$Zn_{0.99}Sn_{0.01}O$	79.23	1.00	19.77	0.01361
$Zn_{0.97}Sn_{0.03}O$	79.27	3.20	17.53	0.03763

agreement with XRD results. Composed entirely of Sn, Zn and O, presented a great degree of purity with the absence of impurities.

Stoichiometric flms of the form $Zn_{1-x}Sn_xO$ were considered. The stoichiometry of the films was determined exclusively at Sn and Zn signal using formula (5):

$$x = \frac{r}{(r+1)} \tag{5}$$

In which x corresponds to the atomic content of Sn and r to the ratio of EDAX signals of Zn and Sn (Table .2). Fig. 4 Showed very clearly the incorporation of tin in the high lattice for all doping levels. It showed the ratio of Sn (EDAX) signals as a function of Sn atomic content calculation, which demonstrated the efficiency of tin doping.

3.4. Fourier transform infrared (FTIR) analysis

FTIR spectrums were investigated in the range of 400–4000 cm^{-1}. Fig. 5, showed a number of clearly characterized peaks appearing at 449, 1020, 2359, 1636, 3450, 2851 and 2931 cm^{-1}. The clearly resolved peak at 449 can be attributed to the vibrational stretching modes of the M − O (Zn–O) bonds, which is the same as reported by Khedidja et al. [46], and Kumar et al. [42,43]. With a shift of this peak position compared to the value of the single crystal (437 cm^{-1}) utilized in approximating the intrinsic stress in the ZnO films [46]. At 1020 cm^{-1} there is a minor peak due to the deformation of C═O. The other peak at 2359 cm^{-1} is attributable to the CO_2 molecules that exist in the air [46].

Two peaks showing up at 3450 cm^{-1} and 1636 cm^{-1} found due to the hydrogen bond vibrations involved in the O–H oscillators in alcohol [44].

Very weak peaks at 2851 cm^{-1}, 2931 cm^{-1}were found and are attributed to *C*–H stretching vibrations of the alkane groups. These specific peaks correlate well with the frequencies of *C*–H_2 symmetric stretching (2855 ± 10 cm^{-1}), *C*–H2 asymmetric stretching (2926 ± 10 cm-1) and *C*–H_3 asymmetric stretching (2962 ± 10 cm-1) vibrations of saturated hydrocarbons, respectively [47–50].

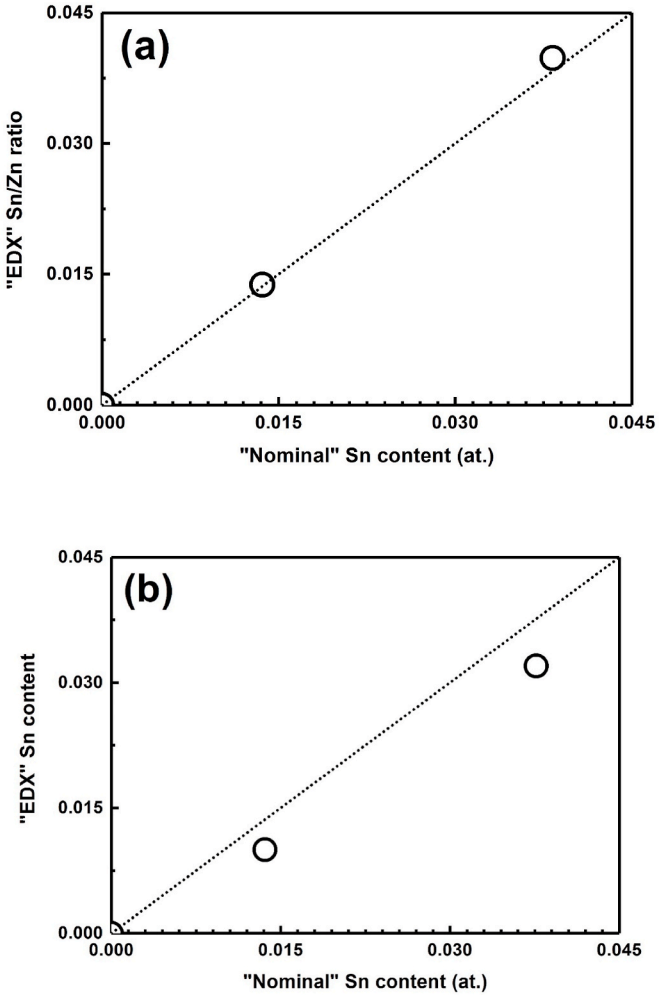

Fig. 4. a) Sn/Zn atomic ratio and b) Sn atomic content (measured with EDAX) plotted as function of the expected Sn content.

3.5. Seebeck coefficient

Fig. 6. Plots the ΔV as a function of temperature gradient for TZO films from 0 to 160 K. Clearly, the values of the Seebeck coefficient were negative. The Seebeck coefficient in a typical metal generally contains contributions from two different mechanisms: thermal diffusion of electrons and phonon drag [51]. If a temperature gradient is available in

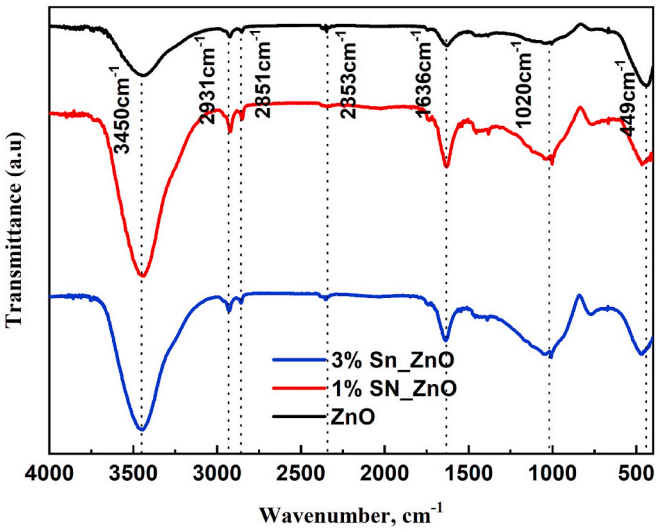

Fig. 5. FTIR spectra of ZnO: Sn thin films in the game 400–4000 cm− 1.

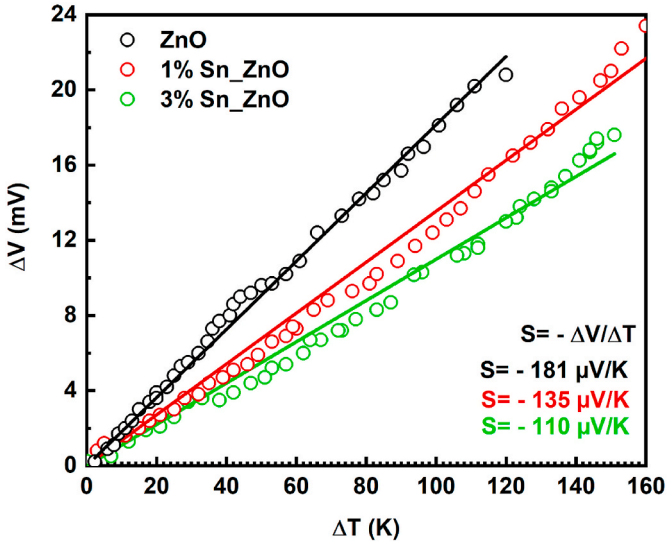

Fig. 6. Seebeck coefficients for ZnO, and Sn-doped ZnO thin films with different Sn concentrations.

a sample, the hotter end electrons will tend to diffuse toward the cooler end, so a thermoelectric potential difference between the hotter and cooler ends ΔV generated. Then, the magnitude of the electric field may be described as, E~ = S ∇ T. S ≈ -ΔV/ΔT is the Seebeck coefficient. The Seebeck coefficients are in the range of −181, −135 and −110 μV/K, for ZnO, Zn0.99Sn0.01O, and Zn0.97Sn0.03O respectively. This negative values of |S| showed the n-type of our pure and doped ZnO films [52]. These results are similar to those of other transparent conducting oxides such as ZnO or In2O3, where Seebeck coefficients in the range of −20 μV/K to −500 μV/K have been determined [53,54].

The Fermi energy (FE) has been calculated by the following equation [51]:

$$E_F = \frac{\pi^2 k_B^2 T}{3|e||S|} \tag{6}$$

where e is the electron charge, kB is the Boltzmann constant and T is the absolute temperature, The Fermi energy values are listed in Fig. 7. The values of Fermi energy decreased by increasing doping content and this could be interpreted by the diffusion of Sn+4 in the ZnO lattice, as

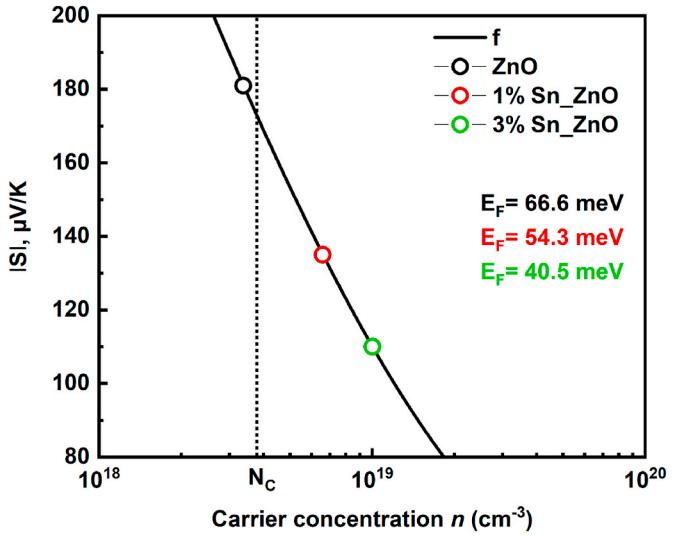

Fig. 7. Seebeck coefficients as a function of carrier concentrations for ZnO and ZnO: Sn thin films.

Sn+4ions will easily replace Zn+2 ions and generate two extra electronic vacancies. As a result, ZnO:Sn films would exhibit good electrical conductivity and will be a suitable material for photovoltaic application.

The carrier concentration has been calculated using the following equations, when

|S|> 75 μV/K [55]:

$$m_S^* = \frac{h^2}{2k_B T}\left\{\frac{3n}{16\sqrt{\pi}}\left(exp\left[\frac{|S|}{(k_B/e)} - 2\right] - 0.17\right)\right\}^{2/3} \tag{7}$$

where e is the carrier charge, kB is the Boltzmann constant, T is the absolute temperature, h is the Planck constant, mS* is the effective Seebeck mass of ZnO, and n is the carrier concentration.

The results of carrier concentration of the Sn-doped ZnO thin films shown in Fig. 7. The Seebeck coefficient and carrier concentration generally have an inverse proportional relationship [56]. In our case, the values of carrier concentration increased with doping level from 3.37 × 1018, to 1.00 × 10^{19} cm^{-3} for ZnO and Zn0.97Sn0.03O films respectively.

Due to the substitution of Sn4+ ions at the site of Zn2+ ions, it results in an increase in the carrier concentration in Sn-doped ZnO than in the undoped ZnO thin films has been observed. Saliha et al. [19] has released analogous results, as well as Hannas et al. who indicated that carrier concentration increased with increasing Sn doping concentration from 1 at.% to 5.0 at.% [57].

To determine the values of the NC the effective density in the conduction band, we have used the expression (7) [58], which interpolate the interval between non-degenerate and degenerate semiconductors, results are shown in Fig. 7.

$$N_C = 2\left(\frac{2\pi m_S^* k_B T}{h^2}\right)^{3/2} \tag{8}$$

There are various studies concerning mS*, including some which consider mS* to be a constant, that is 0.28 m0 for ZnO [59]. In our study, the resulting effective density value of ZnO was 3.71 × 10^{18} cm^{-3}. From the previously calculated carrier concentration values, it was confirmed that the ZnO films were non-degenerate. In contrast Zn0.99Sn0.01O and Zn0.97Sn0.03O films were considered to be degenerated as they contain excess charges compared to the localized states (NC) of ZnO. Resulting of the substitution of some zinc atoms by tin atoms, attributing an

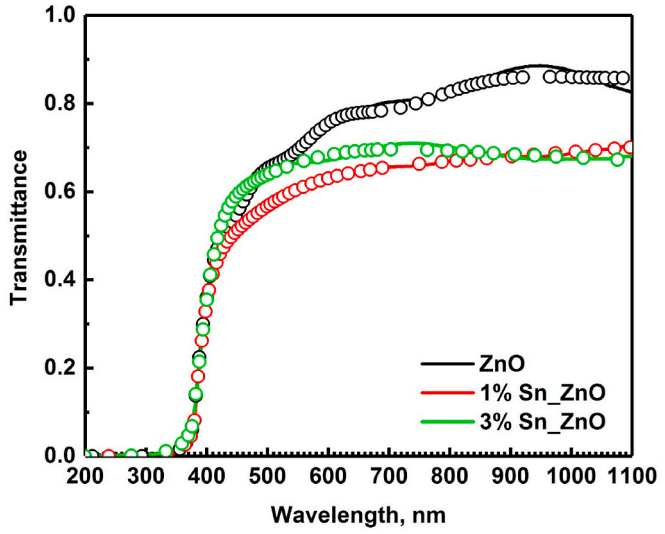

Fig. 8. Transmission spectra of ZnO, TZO thin films deposited on glass substrate at 450 °C. Measured (full circles) and calculated (solid lines) transmittance spectra of films.

increase of the carrier concentration with doping content [60].

3.6. Optical properties

Fig. 8 represents typical transmittance spectra of ZnO, and TZO thin films developed by different concentrations of Sn (1, and 3 at.%) in wavelength range 190–1100 nm. From the transmittance spectra, it can be seen that the transmittance values of our developed thin films varied between 66% and 87% in the visible range. The transmittance decreased with the increasing content of Sn, due to an increase of the photon scattering by the defects of the crystal created by the doping or perhaps because of the progression of the metal/oxygen ratio [41]. In addition, all the layers showed high transmittance in the visible range and with a clear absorption edge at ~381 nm.

The films characteristics were evaluated using a single effect oscillator suggested by Wemple and DiDomenico [61]. The solid curves (Fig. 8) correspond to the fitting curve and the symbols represent the experimental data. The figure showed a good correlation with the experimental data. The values of d, Eg, n at 598 nm, n∞ and E0 extracted by fitting [61] are listed in Table 3.

The width of the band gap was determined from the extrapolation of the linear part of the of the curve representing the function:

$$\alpha h\nu = A\left(h\nu - E_g\right)^{1/2} \tag{9}$$

where hν is the photon energy, Eg is the optical bandgap energy, and A is a constant. We noted that the energy bandgap of TZO tin films was a little higher than that of undoped ZnO layers. As a result, tin, as a dopant of ZnO thin films, can be considered not to change the optical bandgap energy of TZO thin films considerably [60].

The calculated refractive index [61], of Zn1-xSnxO films are shown in Fig. 9. It is interesting that refractive index of films increased with increasing Sn dopant concentration. The refractive index is sensible to structural defects (e.g., voids, dopants, inclusions) [31]. This variation may be due to the incorporation effect of Sn.

The values of the dispersion energy (Ed) were calculated using the formula [61]. Results were reported in Table 3.

$$n_\infty^2 - 1 = \frac{E_d}{E_0} \tag{10}$$

Were E0 is the single oscillator energy and n∞ represents the static refractive index. The values of Eo and Ed for all films increased with doping, that confirmed the substitution of Sn4+ in the ZnO.

The oscillator strengths f for Sn-doped ZnO films were calculated using the relation [62]:

$$f = E_0 E_d \tag{11}$$

The obtained values of f were reported in Table 3. It can be noted that the values of f increased with doping levels as the other optical parameters.

The calculation of the porosity P performed through the optical parameters by applying the Lorentz-Lorenz equation [32].

$$\mathrm{P} = 1 - \left[\left(\mathrm{n}_{\mathrm{film}}^2 - 1\right)\left(\mathrm{n}_{\mathrm{bulk}}^2 + 2\right) \Big/ \left(\mathrm{n}_{\mathrm{film}}^2 + 2\right)\left(\mathrm{n}_{\mathrm{bulk}}^2 - 1\right)\right] \tag{12}$$

Porosity values (Table 3), were less than of pure ZnO, wich could be due to modification in crystal structure. This reduction in porosity resulted in a decrease in adsorption surface area. It can be seen that Zn0.97Sn0.03O films had a higher value than Zn0.99Sn0.10O in agreement with the XRD and SEM results.

3.7. The photocatalytic performance of the Sn-doped ZnO thin films

Fig. 10 (a) illustrated the changes in MB concentration with the increase of irradiation time by utilizing Sn-doped ZnO thin films as photocatalysts. All samples revealed a common tendency, i.e., the MB concentration decreased smoothly with extending irradiation time. Under irradiation, ZnO is absorbing photons and generating electrons and holes. While these electrons and holes can move to the surface of

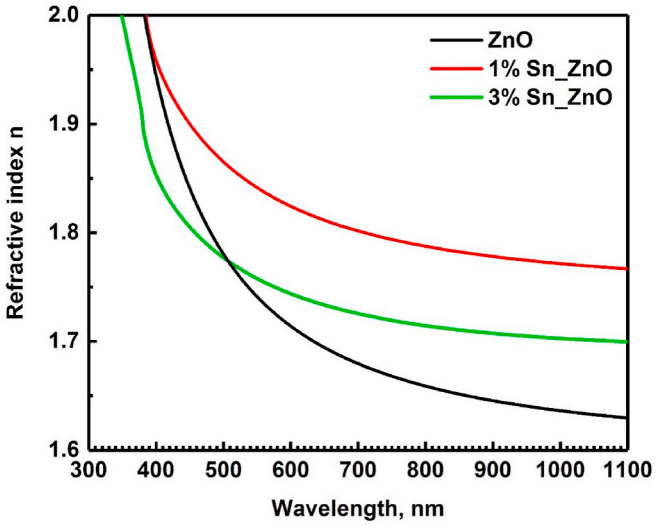

Fig. 9. Refractive index of ZnO, TZO thin films Refractive deposited onto glass substrate at 450 °C.

Table 3
Dispersion parameters of the Sn_ZnO films extracted by fitting the experimental data.

Samples	Thickness (nm)	Eg (eV)	n at 598 nm	n_∞	E_0	E_d	f (eV)^2	P
ZnO	540	3.254	1.71	1.60	4.555	7.10	32.34	0.216
1%Sn_ZnO	150	3.256	1.82	1.74	4.558	7.65	34.86	0.127
3%Sn_ZnO	190	3.258	1.74	1.67	4.561	8.11	36.98	0.191

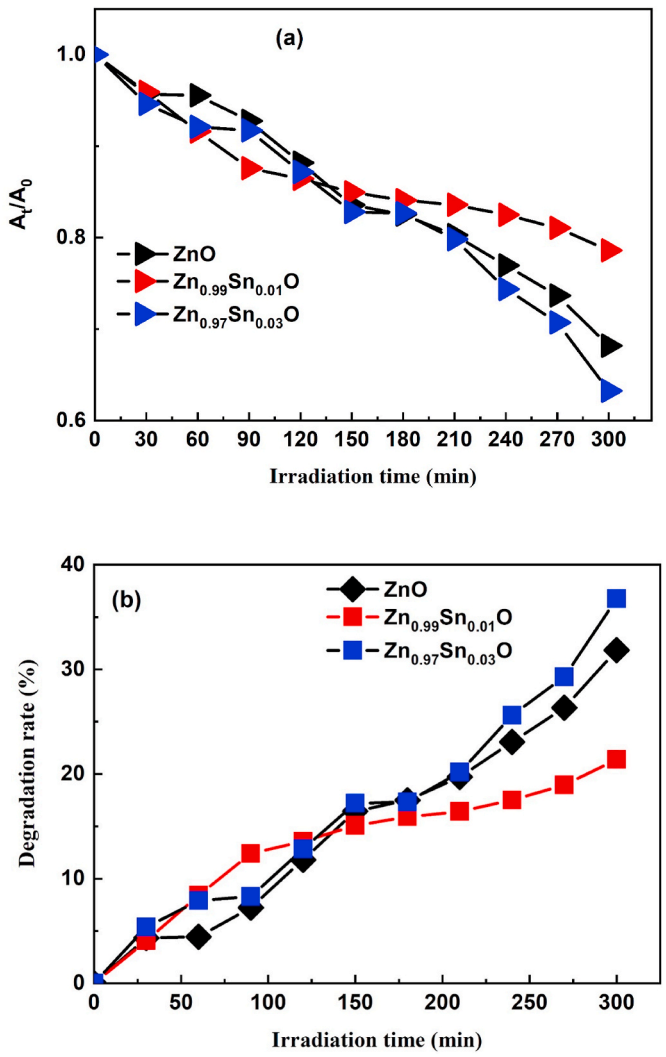

Fig. 10. Photocatalytic activity of ZnO, TZO thin films in MB solution (a), degradation rate of ZnO, TZO thin films in MB solution (b).

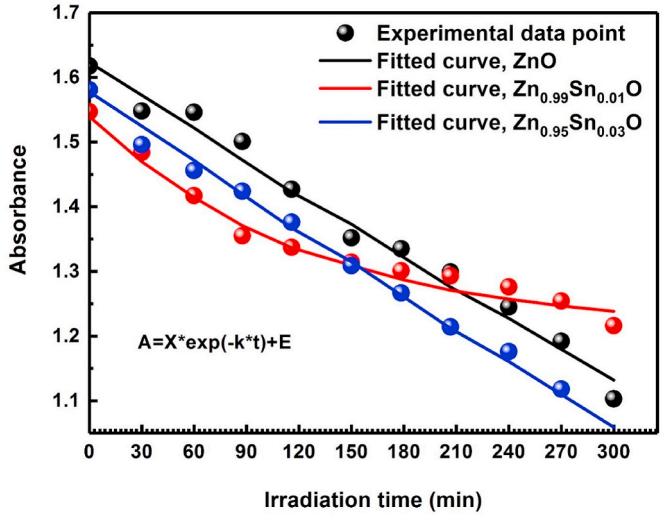

Fig. 11. Degradation kinetics of MB aqueous solutions by ZnO, TZO thin films.

ZnO grains, they will react with water and produce hydroxyl radicals [63–65]. The hydroxyl radicals are powerful oxidizing agent that can degrade organic pollutants. Fig. 10 (a) demonstrated that Sn doping enhanced the photocatalytic performance of ZnO thin films and accelerated photo degradation reaction process.

Fig. 10 (b) showed the degradation rate (%) of the samples under irradiation for 5 h. For the first 120 min, both undoped and Sn-doped ZnO thin films had the same degradation rate (15%), but after this time, the degradation efficiency of the Sn doped ZnO thin films was improved, compared to the undoped ZnO films, especially for the 3 at.% Sn_ZnO samples (38%). As for ZnO (35%) and 1 at.%Sn_ZnO (20%) samples. The improved photodegradation efficiency was expected as a result of the reduced recombination of photogenerated electrons and holes.

The kinetics of the degradation reaction in solution is shown in Fig. 11, and the main calculated kinetic parameters of MB degradation are presented in Table 4, using the following equation (13) [66].

$$A = X * \exp(-k * t) + E \quad (13)$$

While the unit of the (pseudo) rate constant of order k is, the inverse of the unit of time used (min-1), X is the amplitude of the process, E is the end, and both have the same units as the measured quantity A.

It can be seen that the degradation of our dye perfectly followed pseudo first order kinetics. Although the k values for thin films were 0.000244, 0.007857 and 0.000171min-1 for ZnO, 1%Sn_ZnO, and 3% Sn_ZnO respectively. The high k-value of the 1 at.%Sn_ZnO thin films during the first 120min confirmed that the effect of Sn, which improves the separation efficiency of photoinduced charge carriers and optical absorption in the visible region, is the reason for the increase in photocatalytic activity, which is in agreement with the UV–vis results.

Although many factors affect the photocatalytic performance of ZnO thin films, the surface morphology, Crystal structure, the effect of the optical gap [32]. The influence of Sn doping on methylene blue degradation is more complex to interpret in our case. The results showed that Sn-doped ZnO films had the highest number of charge concentration compared to pure ZnO, thus improving the photodegradation process that was mainly resulting from the decrease in the recombination of photogenerated electrons and holes.

The value of the bandgap energy (Eg) of ZnO and TZO thin films were equal, so we could not rely on this factor. One more factor was needed to be clarified was the thickness, we had noticed that the thickness of Sn-doped ZnO thin films was lesser than that of pure ZnO, we could state that there was a proportionality between thickness and photocatalysis.

On the other hand, concerning crystal structure, we had obtained the same structure for both 1%Sn–ZnO and ZnO, but with different thickness (150 and 540 nm) in that order. 3%Sn–ZnO film showed lesser thickness (190 nm). Affecting structure and could be considered as changing the structure, this results confirmed that the thickness and the changes in crystal lattice parameters had affected the MB degradation. The last considered factor was the morphology of thin layers which was changed with an improvement in MB degradation for a doping rate of 3 at.%.

4. Conclusion

Thin films of ZnO and Sn-doped ZnO were deposited by pneumatic spraying technique. A study of the effects of Sn concentration on the structural, microstructural, optical, Seebeck coefficient and photocatalytic properties of the films was carried out. The un-doped and Sn-doped ZnO deposited films showed that the films have a polycrystalline structure that preserves their preferential orientation (002). It is found that 1 at.% is optimum concentration without deterioration of the crystalline and structural properties of ZnO films. The microstructure of the 1% Sn-doped ZnO is rather similar to that of the undoped ZnO film and has spherical grains. By increasing the Sn content more (3%), the films have both small spherical grains. Since the optical

Table 4
Pseudo-first-order kinetic parameters of MB degradation.

Samples	Value			Standard deviation			R^2
	K (min^{-1})	X	E	K (min^{-1})	X	E	
ZnO	0.000244	6.9500	−5.3266	0.00100	27.4072	27.418	0.9844
1% Sn–ZnO	0.007857	0.3326	1.2067	0.00135	0.02079	0.0222	0.9788
3% Sn_ZnO	0.000171	10.3151	−8.7374	0.00146	85.9072	85.924	0.9670

transmittance increases and becomes significant for >381 nm, which proves that Sn-doped ZnO thin films have excellent transparency in the visible range while the optical gap is kept the same with increasing Sn/Zn doping ratio. The Seebeck coefficient was decrease with increasing Sn doping concentration. However, the carrier concentrations increase with the increase of doping content. The results of the application of ZnO and Zn1-xSnxO (x = 1, and 3 at.%), as a photocatalyst for the photo-degradation of methylene blue, indicated that the 3%Sn_ZnO sample is more appropriate for photocatalytic applications.

Declaration of competing interest

The authors declare that they have no known competing financial interests or personal relationships that could have appeared to influence the work reported in this paper.

Acknowledgments

Funding was provided by the General Direction of research and development technologies/Ministry of Higher Education and Research Sciences DGRSDT, MESRS, Algeria. The financial support from Abbes Laghrour University of Khenchela (Algeria). The authors would like to thank the LASPI2A Laboratory of Khenchela University (Algeria) for their financial support of this research project.

References

[1] V. Srikant, D.R. Clarke, J. Mater, Res. 12 (1997) 1425.
[2] M.W. Ahn, K.S. Park, J.H. Heo, D.W. Kim, K.J. Choi, J.G. Park, Sensor. Actuator. B Chem. 138 (2009) 168.
[3] S.H. Jeong, B.N. Park, S.-B. Lee, J.-H. Boo, Thin Solid Films 516 (2008) 5586.
[4] Tsung-Tsong Wu, Wei-Shan Wang, J. Appl. Phys. 96 (2004) 5249–5253.
[5] B. Asengo, A.M. Chaparro, M.T. Gutierrez, J. Herrero, J. Klaer, Sol. Energy Mater. Sol. Cells 87 (2005) 647.
[6] M. Krunks, A. Katerski, T. Dedova, I. Oja Acik, A. Mere, Sol. Energy Mater. Sol. Cells 92 (2008) 1016.
[7] A.D. Acharya, Sh Moghe, R. Panda, S.B. Shrivastava, M. Gangrade, T. Shripathi, D. M. Phase, V. Ganesan, J. Mol. Struct. 1022 (2012) 8.
[8] Y. Caglar, S. Aksoy, S. Ilican, M. Caglar, Superlattice. Microst. 46 (2009) 469.
[9] R.C. Wang, et al., Appl. Phys. Lett. 88 (2006) 23111.
[10] L. Xu, et al., J. Phys. Chem. B 110 (2006) 6637.
[11] M. Vishwas, K.N. Rao, K.A. Gowda, R.P.S. Chakradhar, Spectrochim. Acta Mol. Biomol. Spectrosc. 95 (2012) 423.
[12] J. Li, J. Xu, Q. Xu, G. Fang, J. Alloys Compd 542 (2012) 151.
[13] A.D. Acharya, Shweta Moghe, Richa Panda, S.B. Shrivastava, Mohan Gangrade, T. Shripathi, D.M. Phase, V. Ganesan, J. Mol. Struct. 1022 (2012) 8.
[14] F. Kadi Allah, S. Yapi Abe, C.M. Nunez, A. Khelil, L. Cattin, M. Morsli, J.C. Bernede, A. Bougrine, M.A. del Valle, F.R. Dıaz, Appl. Surf. Sci. 253 (2007) 9241.
[15] S. Ishak, S. Johari, M.M. Ramli, 020027, AIP Conf. Proc. 2203 (2020).
[16] V. Ganesh, I. S. Yahia, S. AlFaify, Mohd. Shkir, J. Phys. Chem. Solids. doi.org/10.1016/j.jpcs.2016.09.022.
[17] S. Ameen Akhtar, M. Shaheer, H.K. Seo, Y.S. Kim, H.S. Shin, Chem. Eng. J. 187 (2012) 351.
[18] N. Ye, J. Qi, Z. Qi, X. Zhang, Y. Yang, J. Liu, Y. Zhang, J. Power Sources 195 (2010) 5806.
[19] S. Ilican, M. Caglar, Y. Caglar, Appl. Surf. Sci. 256 (2010) 7204.
[20] H. Abdullah, M.N. Norazia, S. Shaari, M.Z. Nuawi, N.S. Mohamed Dan, Am. J. Eng. Appl. Sci. 3 (2010) 171.
[21] Linhua Xu, Gaige Zheng, Fenglin Xian, Jing Sua, Mater. Chem. Phys. 229 (2019) 215.
[22] S. Rajeh, A. Barhoumi, A. Mhamdi, G. Leroy, B. Duponchel, M. Amlouk, S. Guermazi, Bull. Mater. Sci. 39 (1) (2016) 177.
[23] S.P. Anthony, J.I. Lee, J.K. Kim, Appl. Phys. Lett. 90 (10) (2007) 103107.
[24] J.J. Wu, S.C. Liu, Adv. Mater 14 (2002) 215.
[25] M.G. Tsoutsouva, C.N. Panagopoulos, D. Papadimitriou, I. Fasaki, M. Kompitsas, Mater. Sci. Eng., B. 176 (2011) 480.
[26] S. Pat, S. Temel, N. Ekem, S. Korkmaz, M. Ozkan, M.Z. Balbaeg, J. Plastic Film Sheeting 27 (2011) 127.
[27] S. Pat, S. Korkmaz, S. Ozen, V. Senay, Part. Sci. Technol. (2018) 1.
[28] M. Kriisa, M. Krunks, E. Kärber, M. Kukk, V. Mikli, A. Mere, J. Nanomater. (2013) 9. Article ID 423632.
[29] S. Roguai, A. Djelloul, Appl. Phys. A 125 (2019) 816.
[30] S. Roguai, A. Djelloul, Appl. Solid State Commun. 334–335 (2021) 114362.
[31] S. Roguai, A. Djelloul, Appl. Phys. A 126 (2020) 122.
[32] S. Roguai, A. Djelloul, React. Kinet. Mech. Catal. 132 (2021) 1225.
[33] M.R. Vaezi, S.K. Sadnezhaad, Mater. Sci. Eng. B 141 (2007) 23.
[34] C.S. Prajapati, A. Kushwaha, P.P. Sahay, Appl. Phys. Mater. Sci. Process 113 (3) (2013) 651.
[35] M.R. Vaezi, S.K. Sadrnezhaad, Mater. Sci. Eng. B 141 (2007) 23.
[36] A. Yildiz, T. Serin, E. Öztürk, N. Serin, Thin Solid Films 522 (2012) 90.
[37] Zi-qiang Xu, H. Deng, Y. Li, Ch Hang, Mater. Sci. Semicond. Process. 9 (2006) 132.
[38] ChY. Tsay, H. Cheng, Y.T. Tung, W.H. Tuan, Ch K. Lin, Thin Solid Films 517 (2008) 1032.
[39] C. Aydin, Sh A. Mansour, Z.A. Alahmed, F. Yakuphanoglu, J. Sol. Gel Sci. Technol. 62 (2012) 397.
[40] C. Aydin, Omar A. Al-Hartomy, A.A. Al-Ghamdi, F. Al-Hazmi, I.S. Yahia, F. El Tantawy, F. Yakuphanoglu, J. Electroceram. 29 (2012) 155.
[41] N. Chahmat, T. Souier, A. Mokri, M. Bououdina, M.S. Aida, M. Ghers, J. Alloys Compd. 593 (2014) 148.
[42] R. Kumar, G. Kumar, M.S. Akhtar, A. Umar, J. Alloys Compd 629 (2015) 167.
[43] R. Kumar, G. Kumar, A. Umar, Mater. Lett. 97 (2013) 100.
[44] H. Bastami, E.Taheri-Nassaj, J. Alloys Compd. 495 (2010) 121.
[45] K. Usha, R. Sivakumar, C. Sanjeeviraja, J. Appl. Phys. 114 (2013) 123501.
[46] Kh Bouzid, A. Djelloul, N. Bouzid, J. Bougdira, Phys. Status Solidi 206 (2009) 106.
[47] N.B. Colthup, L.H. Daly, S.E. Wiberly, Introduction to Infrared and Raman Spectroscopy, third ed., Academic Press, New York, 1990, p. 546.
[48] B. Smith, Infrared Spectral Interpretation, a Systematic Approach, CRC Press, Boca Raton, FL, 1999, p. 265.
[49] N.H. Nickel, K. Fleischer, Phys. Rev. Lett. 90 (2003) 197402.
[50] G.-C. Yi, B.W. Wessels, Appl. Phys. Lett. 70 (1997) 357.
[51] D.K.C. MacDonald, Thermoelectricity: an Introduction to the Principles, Wiley, New York, London, 1962.
[52] T. Tsubota, S. Kobayashi, N. Murakami, T. Ohno, J. Electron. Mater.. DOI: 10.1007/s11664-014-3227-x.
[53] A.Z. Barasheed, S.R.S. Kumar, H.N. Alshareef, J. Mater. Chem. C 1 (2013) 4122.
[54] O. Bierwagen, 024001, Semicond. Sci. Technol. 30 (2015).
[55] A. Zevalkink, D.M. Smiadak, J. Blackburn, A.J. Ferguson, M.L. Chabinyc, O. Delaire, J. Wang, K. Kovnir, J. Martin, L.T. Schelhas, T.D. Sparks, S.D. Kang, M. T. Dylla, G.J. Snyder, B.R. Ortiz, E.S. Tobere, 021303, Appl. Phys. Rev. 5 (2018).
[56] A. Vora-ud, T. Seetawan, W. Somkhunthot, N. Pimpabute, T. Burinprakhon, Energy Proc. 61 (2014) 2355.
[57] M. Hannas, A.K. Shafura, Y. Burhanuddin, S. Alrokayan Majlis, Haseeb A. Khan, M. Rusop, IEEE Student Conference on Research and Development (SCOReD), 2015.
[58] J. Boy, M. Handwerg, R. Ahrling, R. Mitdank, G. Wagner, Z. Galazka, S.F. Fischer, 022526, Apl. Mater. 7 (2019).
[59] J. Ye, S. Gu, S. Zhu, S. Liu, Y. Zheng, R. Zhang, Y. Shi, Appl. Phys. Lett. 86 (2005) 192111.
[60] M. Ajili, M. Castagné, N.K. Turki, Superlattice. Microst. 53 (2013) 213.
[61] S. Roguai, A. Djelloul, C. Nouveau, T. Souier, A.A. Dakhel, M. Bououdina, J. Alloys Compd 599 (2014) 150.
[62] F.Z. Bedia, A. Bedia, N. Maloufi, M. Aillerie, F. Genty, B. Benyouce, J. Alloys Compd. 616 (2014) 312.
[63] N.W.C. Jusoh, A.A. Jalil, S. Triwahyono, A.H. Karim, N.F. Salleh, N.H.R. Annuar, N.F. Jaafar, M.L. Firmansyah, R.R. Mukti, M.W. Ali, Appl. Surf. Sci. 330 (2015) 10.
[64] N. Boussatha, M. Gilliot, H. Ghoualem, J. Martin, Mater. Res. Bull. 99 (2018) 485.
[65] V.K. Jayaraman, A. Hernández-Gordillo, M. Bizarro, Mater. Sci. Semicond. Process. 75 (2018) 36.
[66] Gábor Lente 20, Deterministic Kinetics in Chemistry and Systems Biology vol. 52, Springer, 2015. ISBN 978-3-319-15481-7.